Kinetic Effects of Anion Clusters on the Interfacial Stability between Solid-State Electrolyte and Metal Anode

Hong Fang[1,2,*,†] and Puru Jena[3,‡]

[1] *Department of Physics, Rutgers University, Camden Campus, New Jersey 08102, USA*
[2] *Center for Computational and Integrative Biology, Rutgers University, Camden, New Jersey 08103, USA*
[3] *Department of Physics, Virginia Commonwealth University, Richmond, Virginia 23238, USA*

(Received 30 December 2022; revised 18 October 2023; accepted 15 November 2023; published 7 December 2023)

The success of all-solid-state batteries (ASSBs) depends on the solid-state electrolyte (SSE) exhibiting high interfacial stability and room-temperature ionic conductivity. However, the current SSEs, especially those with practical ionic conductivities ($\geq 10^{-3}$ S/cm) at room temperature, often develop unstable interfaces at the metal anode, in some cases with even greater severity than with liquid organic electrolytes. Despite persistent efforts, achieving interfacial stability and sufficient ionic conductivity simultaneously represents one of the greatest challenges in ASSBs. The current approaches focus on stabilizing the interface by incorporating secondary interlayers or introducing coatings by surface engineering. The method is often material-specific, and the added interlayers often deteriorate during cycling. In this work, using phase analysis and explicit interface modeling, we demonstrate a strategy to kinetically stabilize the interface between the SSE and metal anode by incorporating selected monoanion clusters in the SSE; they can effectively lower or even halt the reduction kinetics at the interface by promoting on-site formation of interphases that are highly electron insulating. The study provides insight into the kinetic effects to achieve SSEs with superior properties in bulk and at the interface.

DOI: 10.1103/PRXEnergy.2.043013

I. INTRODUCTION

One of the greatest challenges in the development of next-generation all-solid-state batteries (ASSBs) is to find solid-state electrolytes (SSEs) with both high ionic conductivities at room temperature and stable electrolyte-electrode interfaces [1]. It is especially essential to have a stable interface when the SSE is coupled with a metal anode to fulfill the promised high energy and high power of the ASSB. However, most SSEs (e.g., sulfides) that exhibit high room-temperature ionic conductivities ($>10^{-3}$ S/cm) are readily reduced by the metal anode, leading to non-self-terminating reaction products at the interface and continuing impedance rise and capacity decay [1,2]. On the other hand, those SSEs (e.g., oxides) that are intrinsically stable against the metal anode often exhibit rather limited ionic conductivities at room temperature. Current efforts to improve the ionic conductivity and interfacial stability are either by surface engineering or incorporating secondary interlayers [3–5].

Besides these chemically oriented approaches, a design paradigm that has attracted a lot of attention recently is the utilization of both the physics (e.g., size, symmetry, motional dynamics, charge distribution, etc.) and the chemistry (e.g., chemical composition, electron affinity, etc.) of anion clusters to greatly enhance the ionic conductivity of the SSEs [6–15]. This design is based on the observation that most SSEs contain anion clusters in their structures, such as polyanions PS_4^{3-}, GeS_4^{3-}, SbS_4^{3-} in sulfides (e.g., $Li_{10}GeP_2S_{12}$, Li_3PS_4, Na_3SbS_4, etc.) and argyrodites (e.g., Li_6PS_5Cl) [16–19], PO_4^{3-}, SiO_4^{4-} in phosphates (e.g., $LiTi_2(PO_4)_3$, $Na_3Zr_2Si_2PO_{12}$, etc.) [20,21], ZrO_6^{8-}, YCl_6^{3-} in oxides (e.g., garnets) and halides (e.g., $Na_{2.25}Y_{0.25}Zr_{0.75}Cl_6$) [22,23], as well as monoanions BH_4^-, $CB_9H_{10}^-$, $CB_{11}H_{12}^-$ in hydrides (e.g., $LiBH_4$, $NaCB_9H_{10}$, $NaCB_{11}H_{12}$, etc.) [24–27]. These anion clusters can either rotate in or form corner-, edge-, or face-sharing frameworks in the lattice, which can significantly facilitate the fast ion diffusion of the SSE due to the dynamic coupling, reduced anion-cation interaction, and enlarged channel space [6,7,10,14,28–30]. Other SSEs that do not include anion clusters often contain halogen elements, such as Li argyrodites (Li_6PS_5X, $X = $ Cl, Br, I),

---

[*] hfangtom@gmail.com
[†] hong.fang@rutgers.edu
[‡] pjena@vcu.edu

Published by the American Physical Society under the terms of the Creative Commons Attribution 4.0 International license. Further distribution of this work must maintain attribution to the author(s) and the published article's title, journal citation, and DOI.

antiperovskites (Li_3OX and Na_3OX, $X = Cl$, Br, I), and halides (e.g., Li_2CdCl_4 and Na_3YCl_6) [19,23,31,32]. According to previous studies, it seems that these halogens inside the SSEs can be readily substituted by monoanion clusters, such as BH_4^-, BF_4^-, CN^-, SCN^-, OH^-, etc., acting like super- or pseudohalogens with proper sizes [33,34]. Once introduced into the lattice, these monoanion clusters can effectively lower the activation energy and promote ionic diffusion according to their uneven sizes, nonspherical shapes, special internal charge distributions, and motional dynamics [6–15]. Their different chemical compositions can also optimize the electronic structure (e.g., band gap) and mechanical properties of the host SSE [10,14,33].

However, most studies so far only focus on improving or optimizing the bulk properties of the SSE using these anion clusters. Effects of anion clusters on the electrolyte-electrode interface are yet to be investigated. In this work, we unravel the special role of anion clusters in the interfacial stability between the SSE and metal anode using a series of cluster-based Li argyrodites as examples. The reason to choose the argyrodite system is that these sulfide SSEs are known for decent room-temperature ionic conductivity but poor stability against a Li metal anode. We show that incorporating selected anion clusters can greatly enhance the stability of the SSE-Li interface by kinetic effects, leading to insights to achieve superior SSEs for ASSBs.

II. RESULTS AND DISCUSSION

It has been shown both in modeling [6,7] and experiments [6,8,11] that it is possible to substitute the halogen component of the Li argyrodite family (Li_6PS_5X, $X = Cl$, Br, I) using monoanion clusters (e.g., BH_4^-, CN^-, etc.) known as super- or pseudohalogens. The sizes of these anion clusters are comparable with those of halogens and they can mimic their chemistry [34]. Based on this, we have developed a class of cluster-based argyrodite SSEs Li_6PS_5Y ($Y = BH_4^-$, BF_4^-, and CN^-). Their ground-state crystal structures are obtained from extensive first-principles structure searches using the particle swarm optimization algorithm (such as the one implemented in CALYPSO [35]) and density-functional theory (DFT) calculations [36,37]. The monoanion cluster involved is treated as a special element with its gas-phase geometry to produce each generation of searched structures. This is done by defining the gas-phase geometry of the cluster using the internal coordinates (*Z* matrix). The monoanion clusters are fully relaxed during the structure optimizations and energy calculation of the search procedure. For each search, an initial population of 40 crystal structures containing the anion cluster are generated according to different structural symmetries and numbers of atoms in the unit cell. The structures are then fully optimized (in both lattice parameters and ion positions) using DFT until the prescribed convergence criteria are met (with the energy difference $<10^{-5}$ eV and forces <0.01 eV/Å). Then, 60% of the optimized structures showing the lowest energies are used to produce the next generation of structures according to their symmetries. The ground-state structures of the cluster-based SSEs are identified after 30 generations of such optimizations. The obtained phases are further tested to for lattice dynamic stability as shown by the calculated phonon spectra in Fig. S1 in the Supplemental Material [38]. It is found that the formation energies corresponding to the reaction $Li_3PS_4 + Li_2S + Li\,Y = Li_6PS_5Y$ with $Y = BH_4^-, BF_4^-$, and CN^- are 8.6, 25, and 15 meV/atom, respectively. These values are smaller than or comparable with the formation energy of 26 meV/atom of Li_6PS_5Cl.

Based on the obtained phases, we first study the electrochemical stability of the cluster-based SSE by constructing the grand potential diagram with the Li metal anode as a lithium reservoir [39–41]. Considering only the kinetics of Li at the interface, the SSE is treated as an open system to the lithium reservoir subject to the range of voltage (V) of the charged cathode against Li^+/Li. The intrinsic electrochemical stability window (ESW) is the voltage range in which the SSE can maintain its original composition against Li insertion or extraction. The grand potential of the active phases is computed as $G = E_0 - \mu_A N_A$, where the Li chemical potential $\mu_A = \mu_0 - eV$, with μ_0 being the chemical potential of the bulk Li and e the electron charge. N_A is the number of Li atoms in a particular phase. E_0 is the DFT-calculated total energy of the phase. Most of these energy values needed in the phase diagram are already available in the Materials Project (MP) database [42]. We calculate the E_0 values for the cluster-based SSEs using the computational parameters that are compatible with the ones used for the MP database, including the Perdew-Burke-Ernzerhof generalized gradient approximation functional [43], projector augmented wave pseudopotentials, spin polarizations, a cutoff energy of 520 eV, and a *k*-point density >1000/atom. The phase diagrams according to different charged voltages (V) are constructed using PYMATGEN [44] with the computed grand potentials.

Based on this, the phase equilibria at the SSE-electrode interface are estimated at different voltages. Figure 1(a) (gray line) shows the obtained Li uptake of the cluster-based SSE $Li_6PS_5(BH_4)$ vs the voltage. At 0 V, $Li_6PS_5(BH_4)$ is reduced by Li metal, producing phase equilibria of $LiB + LiH + Li_2S + Li_3P$. The stable phases of LiB and LiH have close-to-zero band gaps, forming a mixed conducting interphase (MCI) that is both ionically and electronically conductive. It is well known that an MCI cannot effectively passivate the SSE-Li interface [45,46]. With elevated voltage, the SSE keeps taking Li until 1.71 V. It shows a tiny ESW between 1.71 and 1.76 V (with zero Li uptake), and starts being oxidized by giving away Li beyond 1.76 V. According to the same

TABLE I. Bond strength within the studied clusters measured by the bond dissociation energy (D) and force constant (k) obtained by fitting the Morse potential [Eq. (1)] to the bond stretching energies in each case near the equilibrium bond length.

Bond	D (eV)	k (eV/Å^2)
B—H in BH_4^-	2.9	18
B—F in BF_4^-	3.4	28
C—N in CN^-	12.7	109
H—H in H2	4.6	36
C—C in C_2H_6	3.7	24

analysis, $Li_6PS_5(BF_4)$ also shows a tiny ESW between 2.04 and 2.09 V with phase equilibria of LiB + Li_3P + Li_2S + LiF at 0 V (vs Li^+/Li), while $Li_6PS_5(CN)$ shows a zero ESW with phase equilibria of LiC_{12} + Li_2CN_2 + Li_3P + Li_2S at 0 V (vs Li^+/Li). However, such analysis based on the constructed quaternary phase diagrams, e.g., Li-S-P-B-H for $Li_6PS_5(BH_4)$, can be misleading due to the assumption that the monoanion cluster disintegrates into individual elements to form thermodynamically stable phases, such as BH_4^- into B and H to form LiB and LiH, BF_4^- to form LiB and LiF, and CN^- to form LiC_{12} and Li_2CN_2.

In fact, the anion cluster can keep its integrity in the bulk phases owing to its strong internal covalent bonding [6,9,11,47]. To quantify the bond strengths of the studied clusters, a Morse potential [48] is applied to describe the bond stretching energy (E) against the bond length (r),

$$E = D\{1 - \exp[-\alpha(r - r_0)]\}^2, \tag{1}$$

where $\alpha = \sqrt{k/2D}$, with k being the force constant of the bond. D is the dissociation energy of the bond and r_0 is the equilibrium bond length obtained from DFT calculations. The potential energy surface of a single B—X (X = H or F) bond in BH_4^- or BF_4^- or the C—N bond in CN^- is scanned around the equilibrium bond length of each case. The scanned energy data are then fitted by the Morse potential [Eq. (1)] in each case to obtain the bond dissociation energy (D) and the force constant of the bond (k). Good fitting quality together with the dissociation energy and force constant of the bond are obtained for each studied cluster, as shown in Fig. S2 in the Supplemental Material [38]. The estimated dissociation energies and force constants are given in Table I, suggesting that the bond strengths of these clusters are similar to or even greater than those of the typical covalent bonds in H2 and C_2H_6 (as also shown in Table I).

Thus, to correctly evaluate the intrinsic ESW of the cluster-based SSE, the anion cluster should be considered as one of the elementary species in building the phase diagram. This can be done by projecting the phases into a compositional space with the stable salt (e.g., $LiBH_4$ in the current case) occupying one of the vertices of the diagram and forming a pseudoquaternary phase diagram as shown in Fig. 1(b). The corresponding Li uptake vs voltage based on the phase diagrams is shown in Fig. 1(a) (red line). With the BH_4^- intact, the cluster-based SSE exhibits the same ESW as its halogen counterpart Li_6PS_5Cl [41], with a significantly expanded ESW between 1.71 and 2.13 V. At 0 V, $Li_6PS_5(BH_4)$ is still reduced by the Li metal anode. However, its phase equilibria at the interface become $Li(BH_4)$ + Li_2S + Li_3P, where $Li(BH_4)$ is a good electronic insulator (with a band gap >6 eV) which is favorable in passivating the reacting SSE-Li interface.

Explicit interface simulations at finite temperature that can include kinetics of all ion species at the interface are necessary to further understand the effects of the clusters on the stability of the SSE-Li interface. The interface model between the cluster-based SSE and the Li metal is built as a coherent heterointerface, allowing the SSE and Li superlattices to form periodicities along the interfacial plane. Slabs of the SSE and Li metal are cleaved according to different Miller indices (hkl). The lattices of each slab couple are matched according to the epitaxial constraint with the restriction of maximal surface area of 300 Å^2, maximal lattice length mismatch of 0.03 Å, and maximal lattice angle mismatch of 0.01 radians. There are multiple types of terminal species at the interface. The initial distance between the SSE and Li metal slabs are set to 60% of the sum of the van der Waals radii of the terminal elements in close contact. A vacuum padding greater than 13 Å is included to minimize the interaction between the cell images perpendicular to the interface. Table S1 in the Supplemental Material [38] summarizes the built SSE-Li interface models with tiny von Mises strains. The mismatch stresses at the surfaces are smaller than 1 kbar (0.1 GPa). These models are fully optimized and subject to *ab initio* molecular dynamics (AIMD) simulations at room temperature. Each AIMD simulation is performed on the *NVT* ensemble with a time step of 1 fs (to ensure the accuracy of the calculated force at each step). We allow 20 ps of simulation for each system to reach thermal equilibrium before collecting data for another 200 ps for statistical analysis. The current 200 ps simulation time well surpasses the conventional simulation time of 100 ps that has been regularly used to study the interface and bulk properties of solid electrolytes by AIMD [40]. This amount of simulation time is found to be adequate for our current purpose to probe the kinetic stability at the studied interfaces, as demonstrated by the following results. The interface models are built with different surfaces chosen for both SSE and Li metal to ensure the minimum interfacial strain. The long simulation time can help to reduce the possible influence of different surfaces of each substrate on the kinetic reactivity of the interface.

Figure 2(a) shows the as-built interface of $Li_6PS_5(BH_4)$-Li with three possible terminal groups (H2, B, and

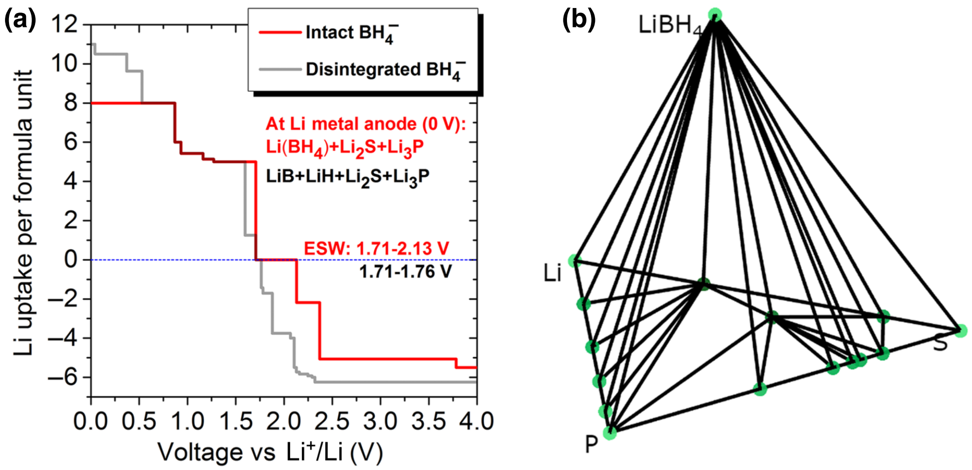

FIG. 1. Intrinsic electrochemical stability of $Li_6PS_5(BH_4)$ evaluated based on the constructed grand potential diagram. (a) Li uptake of the cluster-based SSE against voltage. (b) A constructed pseudoquaternary phase diagram at 0 V with the stable phases shown by the green nodes (including Li_2S, Li_3P, Li_3PS_4, LiS_4, LiP, P_2S_7, P_2S_5, P_4S_9, P_4S_7, Li_3P_7, P_4S_3, and LiP_7).

LiS) in contact with Li metal. We monitor the completeness of the anion clusters PS_4^{3-} and BH_4^- at the interface throughout the simulation. The instability of the cluster-based SSE against Li metal is attributed to the reduction of P in the polyanion PS_4^{3-} contained in the original argyrodite composition, as suggested by the continuing P—S bond breaking in all cases in Fig. 2(b). It is found that the kinetics of reduction reaction in the BH_4-based SSE is significantly slower than that of the lithium argyrodite Li_6PS_5Cl. After 100 ps, the proportion of intact P—S bonds at the Li_6PS_5Cl-Li interface decreases to about 64%, while over 75% of P—S bonds at the $Li_6PS_5(BH_4)$-Li interface remain intact till the end of the simulation. The monoanion BH_4^- is found to be intrinsically stable against Li metal as shown in Fig. 2(b) (black line). Radial distribution function (RDF) analysis reveals the presence of the $Li(BH_4)$ interphase, where the characteristic B—H peaks of $Li(BH_4)$ in the range of 3–5 Å start to appear at the interface (H2) per Fig. 2(c). The formation of the $Li(BH_4)$ interphase accompanies the sluggish reduction of PS_4^{3-}. Among the three $Li_6PS_5(BH_4)$-Li interfaces, the one with the terminal group of LiS [blue line in Fig. 2(b)] shows the slowest reduction kinetics of PS_4^{3-} in the first 50 ps, corresponding to the strongest signal of the interphase $Li(BH_4)$ in its RDF [per Fig. 2(c)]. In contrast, the interface terminated by boron that exhibits little signal of $Li(BH_4)$ shows the fastest reduction kinetics among the three interface models in the first 50 ps, leading to relatively fast P—S

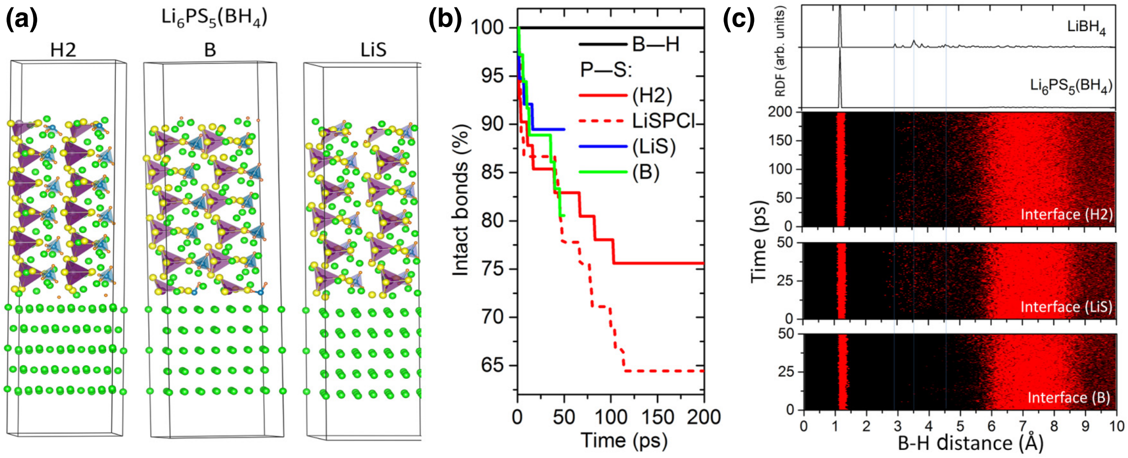

FIG. 2. Explicit modeling for the $Li_6PS_5(BH_4)$-Li interface. (a) The interface models with three possible terminal groups of H2, B, and LiS in close contact with the Li metal. PS_4^{3-} units are in purple tetrahedra, BH_4^- in blue tetrahedra, Li in green, and S in yellow. (b) Percentage of the intact bonds based on the AIMD data. (c) RDF analyses on the interface compared to the bulk phases of $Li_6PS_5(BH_4)$ and $LiBH_4$.

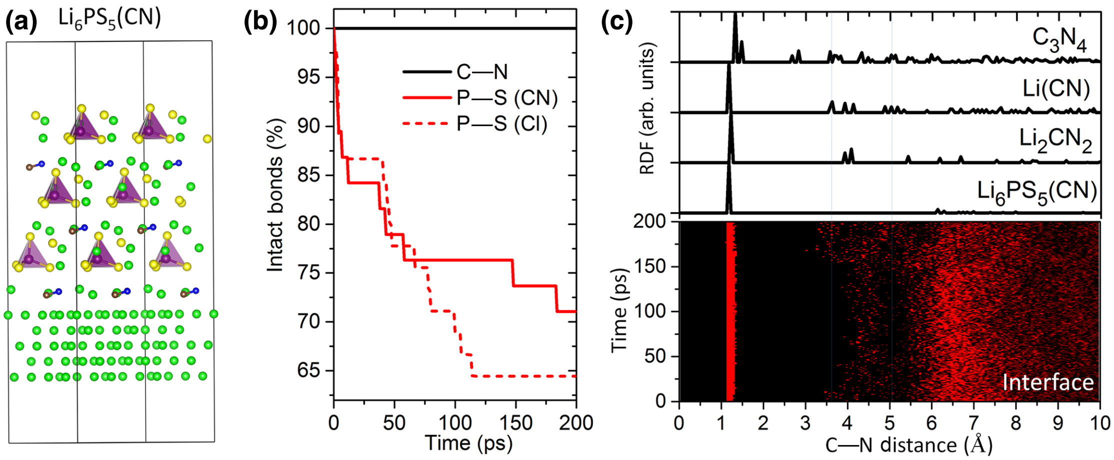

FIG. 3. Explicit modeling for $Li_6PS_5(CN)$-Li interface. (a) Structure of the built interface model, with PS_4^{3-} in purple tetrahedra, CN^- in dumbbells, Li in green, and S in yellow. (b) Percentage of the intact bonds based on the AIMD data.

bond breaking in the same time span, as shown in Fig. 2(b) (green line). These results suggest that reduction kinetics at the interface can be inhibited by the formation of $Li(BH_4)$, which is ionically conductive but electronically insulating [45,46].

Figure 3(a) shows the $Li_6PS_5(CN)$-Li interface model. Again, it is found that the interfacial instability originates from the reduction of polyanions PS_4^{3-} in the argyrodite composition, accompanied by P—S bond breaking. Like the BH_4-based interface, the CN-based interface also shows significantly slower reduction kinetics than that of the Li_6PS_5Cl-Li, maintaining over 70% P—S bonds after 200 ps, as shown in Fig. 3(b). Meanwhile, the monoanion cluster CN^- is intrinsically stable against Li metal. The RDF analysis suggests the formation of a Li(CN) interphase out of a couple of possible stable phases, as shown by the presence of characteristic C—N peaks around 3.5 and 5.0 Å in the RDF of the interface, per Fig. 3(c).

Compared to the previous cases, it is found that the $Li_6PS_5(BF_4)$-Li interface [Fig. 4(a)] becomes stable against Li metal. The reduction of PS_4^{3-} at the $Li_6PS_5(BF_4)$-Li interface quickly stops within 25 ps and about 91% of the P—S bonds remain intact throughout the simulation time, as shown in Fig. 4(b). Like the BH_4^- and CN^- monoanions, BF_4^- is also intrinsically stable against Li metal. The RDF analysis shows the formation of a $Li(BF_4)$ interphase, as suggested by the B—F peaks in the range of 3.5–5 Å in Fig. 4(c). $Li(BF_4)$ has both a very large band gap of 8.2 eV and oxidation potential of 7.1 eV,

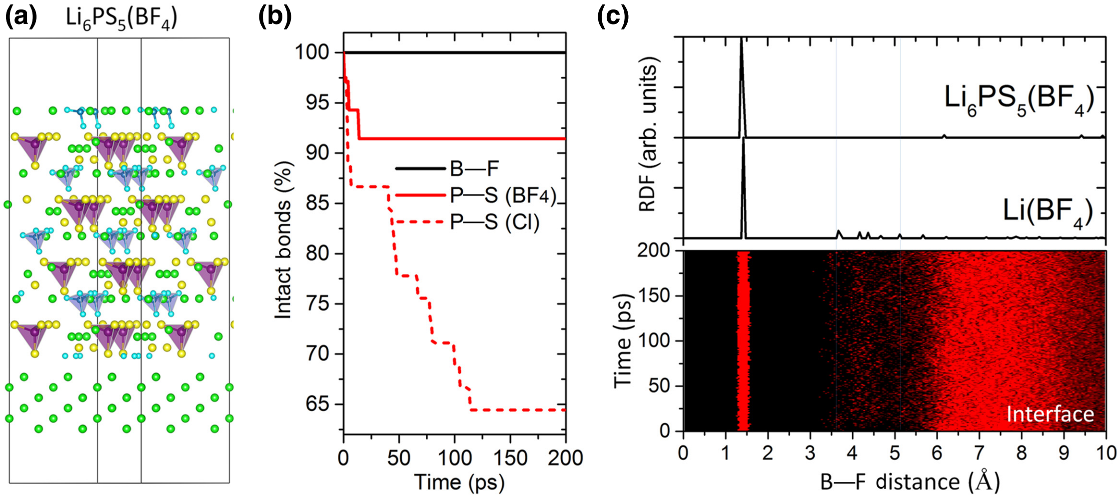

FIG. 4. Explicit modeling for $Li_6PS_5(BF_4)$-Li interface. (a) Structure of the built interface model, with the PS_4^{3-} units in purple tetrahedra, BF_4^- in gray tetrahedra, Li in green, and S in yellow. (b) Percentage of the intact bonds according to the statistical analysis on the AIMD data. (c) RDF analyses on the interface compared to the bulk phases of $Li_6PS_5(BF_4)$ and $LiBF_4$.

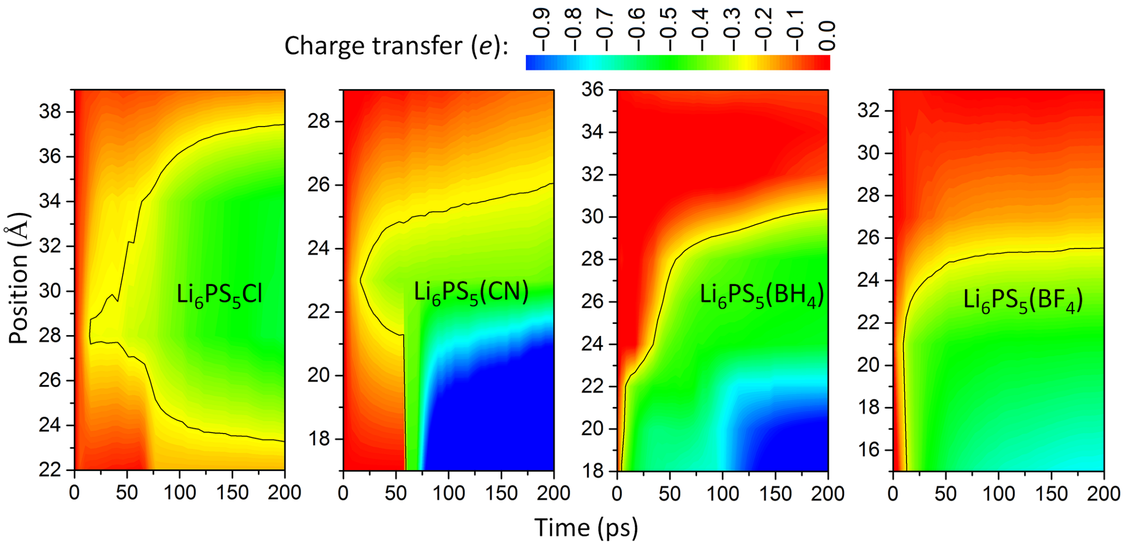

FIG. 5. Direct showing of charge (electron) transfer from Li metal to P in the SSEs. The bottom position (e.g., at 22 Å in the case of Li_6PS_5Cl) corresponds to the top of the Li metal surface in each case. The color bar corresponds to the amount of charge transfer from Li metal to P.

leading to its much stronger ability to kinetically stabilize the SSE-Li interface.

To confirm the kinetic effect of the anion clusters on the interface stability, we have invented an analysis to directly show the charge (electron) transfer out of Li metal that leads to the reduction of P in the SSE. We have written a program that can compute the averaged charge states of P layer by layer in an SSE parallel to the interface surface, using the Bader charges of each "snapshot" structure at certain simulation times from the AIMD data. The obtained charge transfer across the interface against time for each studied case is given in Fig. 5. It is found that the charge transfer from Li metal to P is much more limited in the cluster-based interfaces compared to that in Li_6PS_5Cl-Li. As indicated by the contour lines in the figure, electrons can permeate and distribute across the interphase of Li_6PS_5Cl, while the electrons are only able to concentrate at the bottom of the interphases of the cluster-based SSEs with inhibited charge transfer in both time and space. Indeed, $Li_6PS_5(BF_4)$ with interphase $LiBF_4$ exhibits an exceptional ability of passivation, where the charge transfer quickly peaks and halts after about 25 ps. These results are consistent with the bond analyses in Figs. 2–4.

These results can be further corroborated by the mass transfer across the interface accompanying the charge transfer. Owing to the reduction reaction, Li atoms will diffuse into the SSE and the broken up P from PS_4^{3-} in the SSE will diffuse out of its original crystalline site. These diffusions correspond to the change of atomic distributions across the interface. The atomic distribution of a particular species can be characterized by the position deviation of the atoms along the z axis perpendicular to the interface, defined as,

$$\sigma = \sqrt{\frac{1}{N}\sum_{i=1}^{N}(z_i - \bar{z})^2}, \bar{z} = \frac{1}{N}\sum_{i}^{N} z_i. \tag{2}$$

The change of σ against the simulation time can then measure the change of atomic distributions with time. Figure 6 shows the mass transfer analyses for P and Li, where the distribution of P is roughly maintained at the cluster-based interfaces, while greatly broadened in Li_6PS_5Cl (black line). This corresponds to the sharp decrease of Li distribution in Li_6PS_5Cl due to the merging of Li atoms from the Li metal into the SSE according to the reduction reaction. For the $Li_6PS_5(CN)$ and $Li_6PS_5(BH_4)$ interfaces, the change of Li distribution is rather limited, while the mean distribution of Li for the $Li_6PS_5(BF_4)$ interface is unchanged throughout the time (despite some fluctuations). This again suggests that BF_4^- is the most effective in passivating the interface against Li metal.

Although the Li_6PS_5Cl-Li interface could contain LiCl, which is also a good electronic insulator in its phase equilibria, its much faster reduction reaction than those of the cluster-based interfaces may be due to the following. First, by studying the RDF at the Li_6PS_5Cl-Li interface, it is found that several competing interphases are formed instead of LiCl. As shown in Fig. 7, SCl and SCl_2 that are both thermodynamically stable and experimentally observed [49,50] are identified at the interface according to presence of the continued peaks from 3.3 to 10 Å, compared to the seven discrete peaks of LiCl. In particular, LiCl lacks the interfacial peaks in the range of 3.6 to 4.5 Å as well as the peaks between 5.1 and 6.1 Å, while

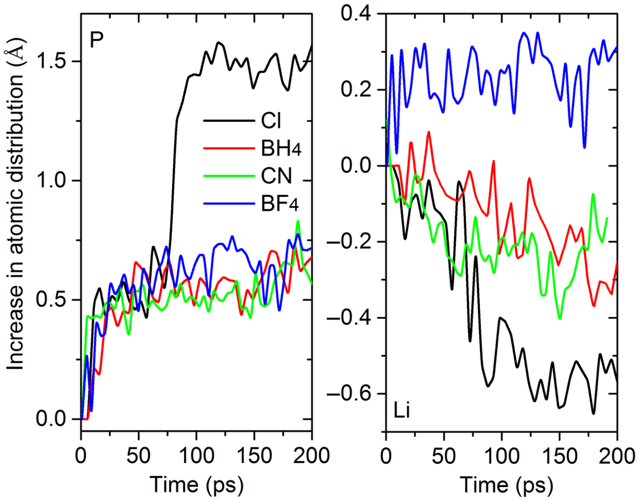

FIG. 6. Change of atomic distribution across the interface measured by the calculated change of atomic deviation (σ).

SCl shows all these characteristic peaks. The band gaps of SCl and SCl_2 are about 2.9 and 2.0 eV, respectively, making them much less effective insulators than LiCl and the cluster-based interphases (with band gaps >6 eV) to inhibit the electron transfer across the interface. Even if LiCl is contained at the Li_6PS_5Cl-Li interface with its RDF signals covered by the broadened peaks of SCl and SCl_2, its quantity should be rather limited due to the presence of the two competing interphases that both cost Cl. In contrast, there are no competing interphases composed of sulfur and the monoanion cluster at the $Li_6PS_5(BH_4)$-Li and $Li_6PS_5(BF_4)$-Li interfaces. The only known stable phases involving sulfur and the composition elements of the monoanion clusters are phases with large boron clusters, including $B_{10}H_{14}S$ [51], B_9H_8S [52], B_5H_7S [51], and BSF_7 [53], which all require disintegration of the BH_4^- and BF_4^- clusters (as shown by their crystal structures in Fig. S3 in the Supplemental Material [38]). This is not the case at all at the cluster-based interfaces, since BH_4^- and BF_4^- are intrinsically stable against Li metal as already shown.

Second, the reaction energy between the halogen-based SSE (with LiCl in its phase equilibria) and Li metal is more negative than those of the cluster-based SSEs. The reaction energies of $Li_6PS_5X + 8Li \rightarrow Li_3P + 5Li_2S + LiX$ at 0 V (vs Li^+/Li) are −0.46, −0.53, and −0.47 eV/atom for $X = BH_4, CN$, and BF_4, respectively, compared to −0.56 eV/atom for $Li_6PS_5Cl + 8Li \rightarrow Li_3P + 5Li_2S + LiCl$. Since the origin of instability at the SSE-Li interface is the continuation of reduction of PS_4^{3-} in the SSE by the Li metal, stabilizing the interface requires inhibiting the electron transfer from Li metal into the bulk SSE across the formed interphases. It is found that the cluster-based interphases exhibit larger band gaps or/and much lower electron mobility than those of LiCl, as shown by the calculated band gaps and the effective electron masses in Table II. Notably, $Li(BF_4)$ has both significantly larger band gap and effective electron mass than LiCl, suggesting a much lower electron mobility in $Li(BF_4)$ than in LiCl. This is consistent with the exceptional stability of the $Li_6PS_5(BF_4)$-Li interface compared with the others. While the $Li(BH_4)$ and Li(CN) interphases can slow the reduction kinetics of PS_4^{3-} at their corresponding interfaces, $Li(BF_4)$ can halt the reduction reaction by effectively stopping the electron transfer from Li metal to the SSE. Note that the electron-insulating properties in the bulk of the halogen-based SSE and the cluster-based SSEs are very similar, as shown in Table II.

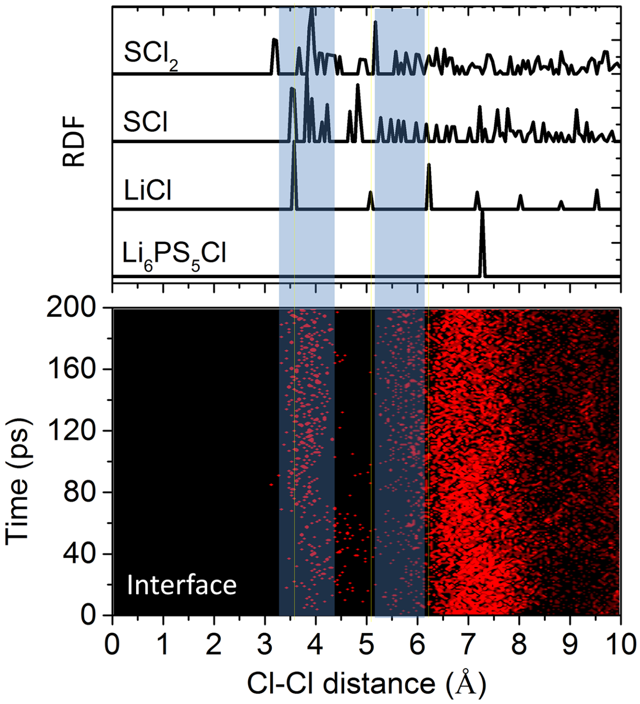

FIG. 7. RDF analysis of the Li_6PS_5Cl-Li interface, compared to the RDFs of the bulk Li_6PS_5Cl, LiCl, SCl, and SCl_2. The shaded areas show the characteristic peaks of SCl matching with the interfacial peaks that are missing in the RDF of LiCl.

TABLE II. Band gaps (BGs) are calculated using hybrid functional HSE06 [54] to ensure accuracy. The electron effective masses (EEM) are calculated at the Γ point with respect to the wave vector $\boldsymbol{k}$ along the three crystallographic directions, with second derivatives of energy numerically calculated with the finite-difference method.

SSEs	SSE BG (eV)	SSE EEM (m_e)	Interphase	BG (eV)	EEM (m_e)
Li_6PS_5Cl	3.4	0.43	LiCl	6.22	0.59
$Li_6PS_5(BH_4)$	3.3	0.43	$Li(BH_4)$	6.37	0.85
$Li_6PS_5(CN)$	3.2	0.43	Li(CN)	5.53	1.41
$Li_6PS_5(BF_4)$	3.5	0.44	$Li(BF_4)$	8.25	0.72

III. CONCLUSION

We find that incorporating selected monoanion clusters, such as BH_4^- and BF_4^-, in SSEs can significantly enhance the stability of the SSE-Li interface that would otherwise decay due to reduction of the SSE by Li metal. This is achieved because of the intrinsic stability and the chemistry of the clusters, preventing the clusters from forming undesired competing interphases with the active species at the interface. Meanwhile, the cluster-induced on-site formation of ionically conductive and electronically insulating interphases can effectively lower the reduction kinetics at the interface. In particular, the BF_4^--based SSE $Li_6PS_5(BF_4)$ shows a stable interface against Li metal due to the exceptionally low electron mobility of the BF_4^--containing phases. This is in contrast with the halogen-based lithium argyrodite, where interphases between halogen and sulfur are likely to form with less-effective electron-insulating ability. In addition, recent computational and experimental studies [6–15] have already proved that introducing these monoanion clusters into the SSEs can significantly improve the ion diffusivity. The current insights into the kinetic effects of anion clusters on the interfacial stability show that using clusters as the building blocks of SSEs is a promising strategy to simultaneously achieve both high ionic conductivity and high interfacial stability. For example, a recent study showed that the BF_4^--containing antiperovskite $Li_3S(BF_4)_{0.5}Cl_{0.5}$ SSE with high Li diffusivity [14] is effective in stabilizing electrodeposition and suppressing dendrite growth of Li at the interface [55]. Such a strategy can be readily applied to a broad range of SSEs based on lithium, sodium, and potassium. The current study also demonstrates the importance of explicit interface modeling covering the kinetics of all active species. Without such explicit simulations, one would not be able to identify the interphases that are likely to form at the Li_6PS_5Cl-Liinterface, such as SCl and SCl_2 instead of LiCl. The explicit interface modeling is especially important for a cluster-based system, where the ion kinetics plays a central role in determining the interfacial stability. It would be interesting to see in follow-up studies how the interfaces will evolve based on large-scale modeling with a time scale of tens to hundreds of nanoseconds using accurate force fields.

ACKNOWLEDGMENTS

The work is supported by the U.S. Department of Energy, Office of Energy Efficiency and Renewable Energy Award No. DE-EE0008865 (H.F. and P.J.), Battery500 Seedling Project Contract No. 674882 (H.F. and P.J.), and the U.S. Department of Energy, Basic Energy Sciences, Division of Materials Sciences and Engineering under Award No. DE-FG02-96ER45579 (P.J.). Resources from the National Energy Research Scientific Computing Center supported by the Office of Science of the U.S. Department of Energy under Contract No. DE-AC02-05CH11231 and from the National Renewable Energy Laboratory High-Performance Computing Facilities (with Kestrel and Swift computing systems) are also acknowledged (H.F. and P.J.).

[1] X. Feng, H. Fang, N. Wu, P. Liu, P. Jena, J. Nanda, and D. Mitlin, Review of modification strategies in emerging inorganic solid-state electrolytes for lithium, sodium, and potassium batteries, Joule **6**, 543 (2022).

[2] V. Lacivita, Y. Wang, S.-H. Bo, and G. Ceder, Ab initio investigation of the stability of electrolyte/electrode interfaces in all-solid-state Na batteries, J. Mater. Chem. A **7**, 8144 (2019).

[3] Y. Tian, Y. Sun, D. C. Hannah, Y. Xiao, H. Liu, K. W. Chapman, S.-H. Bo, and G. Ceder, Reactivity-guided interface design in Na metal solid-state batteries, Joule **3**, 1037 (2019).

[4] S. Zhang, Y. Zhao, F. Zhao, L. Zhang, C. Wang, X. Li, J. Liang, W. Li, Q. Sun, C. Yu, *et al.*, Gradiently sodiated alucone as an interfacial stabilizing strategy for solid-state Na metal batteries, Adv. Funct. Mater. **30**, 2001118 (2020).

[5] X. Feng, H. Fang, P. Liu, N. Wu, E. C. Self, L. Yin, P. Wang, X. Li, P. Jena, J. Nanda, and D. Mitlin, Heavily tungsten-doped sodium thioantimonate solid-state electrolytes with exceptionally low activation energy for ionic diffusion, Angew. Chem. **133**, 26362 (2021).

[6] Y. Sun, B. Ouyang, Y. Wang, Y. Zhang, S. Sun, Z. Cai, V. Lacivita, Y. Guo, and G. Ceder, Enhanced ionic conductivity and lack of paddle-wheel effect in pseudohalogen-substituted Li argyrodites, Matter **5**, 4379 (2022).

[7] H. Fang and P. Jena, Argyrodite-type advanced lithium conductors and transport mechanisms beyond paddle-wheel effect, Nat. Commun. **13**, 2078 (2022).

[8] A. E. Maughan, Y. Ha, R. T. Pekarek, and C. M. Schulze, Lowering the activation barriers for lithium-ion conductivity through orientational disorder in the cyanide argyrodite Li_6PS_5CN, Chem. Mater. **33**, 5127 (2021).

[9] Y. Sun, Y. Wang, X. Liang, Y. Xia, L. Peng, H. Jia, H. Li, L. Bai, J. Feng, H. Jiang, and J. Xie, Rotational cluster anion enabling superionic conductivity in sodium-rich antiperovskite Na_3OBH_4, J. Am. Chem. Soc. **141**, 5640 (2019).

[10] H. Fang and P. Jena, Sodium superionic conductors based on clusters, ACS Appl. Mater. Interfaces **11**, 963 (2019).

[11] A. Sakuda, A. Yamauchi, S. Yubuchi, N. Kitamura, Y. Idemoto, A. Hayashi, and M. Tatsumisago, Mechanochemically prepared $Li_2S-P_2S_5-LiBH_4$ solid electrolytes with an argyrodite structure, ACS Omega **3**, 5453 (2018).

[12] K. E. Kweon, J. B. Varley, P. Shea, N. Adelstein, P. Mehta, T. W. Heo, T. J. Udovic, V. Stavila, and B. C. Wood, Structural, chemical, and dynamical frustration: origins of superionic conductivity in closo-borate solid electrolytes, Chem. Mater. **29**, 9142 (2017).

[13] H. Fang, S. Wang, J. Liu, Q. Sun, and P. Jena, Superhalogen-based Li-ion superionic conductors, J. Mater. Chem. A **5**, 13373 (2017).

[14] H. Fang and P. Jena, Li-rich antiperovskite superionic conductors based on cluster ions, Proc. Natl. Acad. Sci. **14,** 1047 (2017).

[15] W. S. Tang, A. Unemoto, W. Zhou, V. Stavila, M. Matsuo, H. Wu, S. Orimo, and T. J. Udovic, Unparalleled lithium and sodium superionic conduction in solid electrolytes with large monovalent cage-like anions, Energy Environ. Sci. **8,** 3637 (2015).

[16] N. Kamaya, K. Homma, Y. Yamakawa, M. Hirayama, R. Kanno, M. Yonemura, T. Kamiyama, Y. Kato, S. Hama, and K. Kawamoto, A lithium superionic conductor, Nat. Mater. **10,** 682 (2011).

[17] R. Kanno and M. Murayama, Lithium ionic conductor thio-LISICON: The $Li_2SGeS_2P_2S_5$ system, J. Electrochem. Soc. **148,** A742 (2001).

[18] Q. Zhang, C. Zhang, Z. D. Hood, M. Chi, C. Liang, N. H. Jalarvo, M. Yu, and H. Wang, Abnormally low activation energy in cubic Na_3SbS_4 superionic conductors, Chem. Mater. **32,** 2264 (2020).

[19] H.-J. Deiseroth, S.-T. Kong, H. Eckert, J. Vannahme, C. Reiner, T. Zaiß, and M. Schlosser, Li_6PS_5X: A class of crystalline Li-rich solids with an unusually high Li^+ mobility, Angew. Chem., Int. Ed. **47,** 755 (2008).

[20] A. Martínez-Juarez, C. Pecharroman, J. E. Iglesias, and J. M. Rojo, Relationship between activation energy and bottleneck size for Li^+ ion conduction in NASICON materials of composition $LiMM'(-PO_4)_3$; M, M′ = Ge, Ti, Sn, Hf, J. Phys. Chem. B **102,** 372 (1998).

[21] A. G. Jolley, G. Cohn, G. T. Hitz, and E. D. Wachsman, Improving the ionic conductivity of NASICON through aliovalent cation substitution of $Na_3Zr_2SiPO_{12}$, Ionics **21,** 3031 (2015).

[22] C. Bernuy-Lopez, W. Manalastas, J. M. Lopez del Amo, A. Aguadero, F. Aguesse, and J. A. Kilner, Atmosphere controlled processing of Ga-substituted garnets for high Li-ion conductivity ceramics, Chem. Mater. **26,** 3610 (2014).

[23] E. A. Wu, S. Banerjee, H. Tang, P. M. Richardson, J.-M. Doux, J. Qi, Z. Zhu, A. Grenier, Y. Li, E. Zhao, *et al.*, A stable cathode-solid electrolyte composite for high-voltage, long-cycle-life solid-state sodium-ion batteries, Nat. Commun. **12,** 1256 (2021).

[24] H. Maekawa, M. Matsuo, H. Takamura, M. Ando, Y. Noda, T. Karahashi, and S.-i Orimo, Halide-stabilized $LiBH_4$, a room-temperature lithium fast-ion conductor, J. Am. Chem. Soc. **131,** 894 (2009).

[25] F. Murgia, M. Brighi, L. Piveteau, C. E. Avalos, V. Gulino, M. C. Nierstenhöfer, P. Ngene, P. Jongh, and R. Černý, Enhanced room-temperature ionic conductivity of $NaCB_{11}H_{12}$ via high-energy mechanical milling, ACS Appl. Mater. Interfaces **13,** 61346 (2021).

[26] W. S. Tang, M. Matsuo, H. Wu, V. Stavila, W. Zhou, A. A. Talin, A. V. Soloninin, R. V. Skoryunov, O. A. Babanova, A. V. Skripov, *et al.*, Liquid-like ionic conduction in solid lithium and sodium monocarba-closo-decaborates near or at room temperature, Adv. Energy Mater. **6,** 1502237 (2016).

[27] X. Luo, A. Rawal, and K.-F. Aguey-Zinsou, Investigating the factors affecting the ionic conduction in nanoconfined $NaBH_4$, Inorganics **9,** 2 (2021).

[28] J. G. Smith and D. J. Siegel, Low-temperature paddlewheel effect in glassy solid electrolytes, Nat. Commun. **11,** 1483 (2020).

[29] Z. Zhang, P.-N. Roy, H. Li, M. Avdeev, and L. F. Nazar, Coupled cation-anion dynamics enhances cation mobility in room-temperature superionic solid-state electrolytes, J. Am. Chem. Soc. **141,** 19360 (2019).

[30] K. Jun, Y. Sun, Y. Xiao, Y. Zeng, R. Kim, H. Kim, L. J. Miara, D. Im, Y. Wang, and G. Ceder, Lithium superionic conductors with corner-sharing frameworks, Nat. Mater. **21,** 924 (2022).

[31] Y. Zhao and L. L. Daemen, Superionic conductivity in lithium-rich anti-perovskites, J. Am. Chem. Soc. **134,** 15042 (2012).

[32] H. D. Lutz, W. Schmidt, and H. Haeuseler, Chloride spinels: A new group of solid lithium electrolytes, J. Phys. Chem. Solids **42,** 287 (1981).

[33] H. Fang and P. Jena, Atomic-level design of water-resistant hybrid perovskites for solar cells by using cluster ions, J. Phys. Chem. Lett. **8,** 3726 (2017).

[34] H. Fang and P. Jena, Super-ion inspired colorful hybrid perovskite solar cells, J. Mater. Chem. A **4,** 4728 (2016).

[35] Y. Wang, J. Lv, L. Zhu, and Y. Ma, Crystal structure prediction via particle swarm optimization, Phys. Rev. B **82,** 094116 (2010).

[36] G. Kresse and J. Furthmueller, Efficiency of ab-initio total energy calculations for metals and semiconductors using a plane-wave basis set, J. Comput. Mater. Sci. **6,** 15 (1996).

[37] G. Kresse and J. Furthmueller, Efficient iterative schemes for ab initio total-energy calculations using a plane-wave basis set, Phys. Rev. B. **54,** 11169 (1996).

[38] See Supplemental Material at http://link.aps.org/supplemental/10.1103/PRXEnergy.2.043013 for the calculated phonon spectra of the cluster-based solid-state electrolytes, the scanned potential energy surface of bonds for each studied cluster fitted by the Morse potential, the unit cells of the stable phases involving sulfur and the elements of the monoanion clusters, and the built coherent interfacial models for the cluster-based solid electrolytes and Li metal anode.

[39] S. P. Ong, L. Wang, B. Kang, and G. Ceder, Li-Fe-P-O_2 phase diagram from first principles calculations, Chem. Mater. **20,** 1798 (2008).

[40] H. Tang, Z. Deng, Z. Lin, Z. Wang, I.-H. Chu, C. Chen, Z. Zhu, C. Zheng, and S. P. Ong, Probing solid-solid interfacial reactions in all-solid-state sodium-ion batteries with first-principles calculations, Chem. Mater. **30,** 163 (2018).

[41] Z. Deng, Z. Zhu, I.-H. Chu, and S. P. Ong, Data-driven first-principles methods for the study and design of alkali superionic conductors, Chem. Mater. **29,** 281 (2017).

[42] A. Jain, S. P. Ong, G. Hautier, W. Chen, W. D. Richards, S. Dacek, S. Cholia, D. Gunter, D. Skinner, G. Ceder, and K. A. Persson, Commentary: The Materials Project: A materials genome approach to accelerating materials innovation, APL Mater. **1,** 011002 (2013).

[43] J. P. Pewdew, K. Burke, and M. Ernzerhof, Generalized gradient approximation made simple, Phys. Rev. Lett. **77,** 3865 (1996).

[44] S. P. Ong, W. D. Richards, A. Jain, G. Hautier, M. Kocher, S. Cholia, D. Gunter, V. L. Chevrier, K. A. Persson, and

G. Ceder, Python materials genomics (pymatgen): a robust, open-source python library for materials analysis, Comput. Mater. Sci. **68**, 314 (2013).

[45] Y. Zhu, X. He, and Y. Mo, Origin of outstanding stability in the lithium solid electrolyte materials: insights from thermodynamic analysis based on first-principles calculations, ACS. Appl. Mater. Interfaces **7**, 23685 (2015).

[46] Y. Li, P. Canepa, and P. Gorai, Role of electronic passivation in stabilizing the lithium-$Li_xPO_yN_z$ solid-electrolyte interphase, PRX Energy **1**, 023004 (2022).

[47] H. Fang and P. Jena, Stable tetra- and penta-anions in the gas phase, Angew. Chem., Int. Ed. **58**, 11248 (2014).

[48] P. M. Morse, Diatomic molecules according to the wave mechanics. II. Vibrational levels, Phys. Rev. **34**, 57 (1929).

[49] R. Kniep, L. Korte, and D. Mootz, Kristallstrukturen von verbindungen A_2X_2 ($A = S$, Se; $X = Cl$, Br), Z. Naturforsch., B: Anorg. Chem., Org. Chem. **38**, 1 (1983).

[50] R. Kniep, L. Korte, and D. Mootz, Phase relations in the system sulfur-chlorine and crystal structures of SCl_2 and SCl_4, Z. Naturforsch., B: Anorg. Chem., Org. Chem. **39**, 305 (1984).

[51] J. Bould, J. Machacek, M. G. S. Londesborough, R. Macias, J. D. Kennedy, Z. Bastl, P. Rupper, and T. Base, Decaborane thiols as building blocks for self-assembled monolayers on metal surfaces, Inorg. Chem. **51**, 1685 (2012).

[52] W. R. Pretzer, T. K. Hilty, and R. W. Rudolph, Crystal and molecular structure of 2,2'-bis(1-thia-closo-decaborane(8)), 2,2'-$(1\text{-}B_9H_8S)_2$, Inorg. Chem. **14**, 2459 (1975).

[53] D. D. Gibler, C. J. Adams, M. Fischer, A. Zalkin, and N. Bartlett, Structural studies of trifluorosulfur(iv)yl, $(SF_3)^+$, salts including the crystal structure of $(SF_3)^+(BF_4)^-$, Inorg. Chem. **11**, 2325 (1972).

[54] J. Heyd and G. Scuseria, Efficient hybrid density functional calculations in solids: The HS-Ernzerhof screened Coulomb hybrid functional, J. Chem. Phys. **121**, 1187 (2004).

[55] W. Li, H. A. Tchelepi, and D. M. Tartakovsky, Screening of electrolyte-anode buffers to suppress lithium dendrite growth in all-solid-state batteries, J. Electrochem. Soc. **170**, 050510 (2023).